An open-architecture metal powder bed fusion system for in-situ process measurements

BIDARE, Prveen, MAIER, RRJ, BECK, RJ, SHEPHARD, JD and MOORE, AJ

Citation:

BIDARE, Prveen, MAIER, RRJ, BECK, RJ, SHEPHARD, JD and MOORE, AJ (2017). An open-architecture metal powder bed fusion system for in-situ process measurements. Additive Manufacturing, 16, 177-185. [Article]

Additive Manufacturing 16 (2017) 177–185

Contents lists available at ScienceDirect

Additive Manufacturing

journal homepage: www.elsevier.com/locate/addma

Full Length Article

An open-architecture metal powder bed fusion system for in-situ process measurements

P. Bidare*, R.R.J. Maier, R.J. Beck, J.D. Shephard, A.J. Moore

Institute of Photonics and Quantum Sciences, School of Engineering and Physical Sciences, Heriot-Watt University, Edinburgh, EH14 4AS, UK

ARTICLE INFO

Article history:
Received 28 December 2016
Received in revised form 27 March 2017
Accepted 15 June 2017
Available online 17 June 2017

Keyword:
Powder bed fusion
Selective laser melting
In-situ measurements
Density measurements
Powder consolidation measurements

ABSTRACT

We report the design of a metal powder bed fusion system for in-situ monitoring of the build process during additive manufacture. Its open-architecture design was originally determined to enable access for x-rays to the melt pool, but it also provides access to the build area for a range of other in-situ measurement techniques. The system is sufficiently automated to enable single tracks and high-density, multiple layer components to be built. It is easily transportable to enable measurements at different measurement facilities and its modular design enables straightforward modification for the specific measurements being made. We demonstrate that the system produces components with >99% density. Hence the build conditions are representative to observe process fundamentals and to develop process control strategies.

1. Introduction

Metal powder bed fusion (PBF) is a well-known process category in additive manufacture (AM) in which thermal energy selectively fuses regions of a powder bed [1]. It is sometimes referred to by manufacturers' names, for example selective laser melting (SLM) and direct metal laser sintering (DMLS). The PBF system described in this paper was designed as part of a feasibility study to use x-rays for in-situ imaging of the melt pool during metal PBF. The open-architecture design of the system also enables flexible access for other process measurements in addition to x-ray imaging, including high-speed imaging, shield gas flow and temperature. In this paper we describe the design of the open-architecture PBF system and validate its performance. The results of specific process monitoring applications, and the understanding of process fundamentals provided by them, will be reported elsewhere.

The design of the PBF system was determined by the requirements for x-ray access. The aim of the x-ray measurements in the feasibility study is to yield process understanding, rather than validating the quality of parts during their build. Such images will yield new insight into the physical processes that occur during PBF, including the powder melting and solidifying, fluid dynamics in the melt-pool and the formation of pores. One example where this insight might be useful is in improving the high-cycle fatigue life of titanium components produced by AM, which is dominated by cracks that nucleate at near-surface pores. Many factors can contribute to pore formation, including instability of the melt pool [2], lack of fusion between powder particles [3,4], the laser keyhole leaving a trail of voids [5], narrow powder particle size distribution reducing the packing in a layer [6,7], scanning strategy with insufficient overlap between adjacent tracks [8,9] and spatter and oxidation due to lack of shielding gas [10]. A better systematic understanding of the relationships between the process parameters and the size, density, and three-dimensional spatial distribution of pores might be used to eliminate their detrimental effect on fatigue life, without resorting to additional costly process steps such as hot isostatic pressing.

X-ray access to the powder bed is extremely difficult in a commercial PBF machine. Obviously the complex and compact machinery is not optimized for x-ray passage to the powder bed and modifications to the powder delivery system, build platform and laser delivery would be prohibitively expensive. Bespoke PBF systems to implement process monitoring and imaging have been reported. Craeghs et al. [11] developed a PBF system for real-time melt pool monitoring to see in-situ process defects; Sercombe et al. [12] reported post-process x-ray micro-tomography measurements of the deformation and failure of scaffolds; Vlasea et al. [13] proposed the design of a PBF system to asses in-process monitoring techniques and intermittent metrology of the powder bed between layers; Land et al. [14] discussed a PBF system fitted with non-contact metrology systems to measure layer characteristics to

---

* Corresponding author.
E-mail address: bidarep@gmail.com (P. Bidare).

http://dx.doi.org/10.1016/j.addma.2017.06.007

be compared with the final components. None of these systems has been designed for in-process x-ray imaging.

2. Requirements for the PBF system

Our objective is to record in-process x-ray images around the melt pool in a metal powder bed. We are interested in imaging a region ~500 μm long that incorporates the melt pool with un-melted powder in front and solidifying material behind. Of particular importance is realistic heat conduction away from the melt-pool and for the ability to monitor pores through multiple build layers. A short exposure time is required to effectively freeze the motion of the melt-pool as it moves across the powder bed at speeds up to several hundred mm/s. Successful x-ray imaging therefore requires that:

- the intensity of the x-ray source is sufficient to record short exposure images through the build plate and any other metal in the beam path;
- the spatial resolution is sufficient (~1 μm) for individual powder particles to be imaged;
- the image contrast is sufficient to resolve small variations in x-ray absorption in the powder layer above noise in the image.

X-ray sources with these characteristics can be set up at the Science and Technology Facilities Council Central Laser Facility (STFC CLF) in the UK. The ultra-high intensity Vulcan laser (power ~10^{15} W, light intensity 10^{21} W/cm^2 pulses) can drive a compact particle accelerator when focussed on a solid foil target [15]. The short laser pulse (~few ps) produces a plasma and drives electrons at relativistic energies through the foil. These electrons interact with the solid material of the foil to generate high-energy bremsstrahlung x-rays that emerge from the rear surface of the foil in a diverging cone from a spot of less than 100 μm across. These x-rays have a broad energy spectrum (10's keV to 5 MeV), a duration of a few picoseconds and sufficient intensity to record projection images through thick metallic objects [16,17]. The time between x-ray pulses is ~15 min, determined by the repetition rate of Vulcan laser. The diverging x-ray beam emerges horizontally into a test room, with an included angle of approximately 40°. The operator is stationed in a separate control room to avoid exposure to the burst of x-rays, gamma rays and charged particles produced by the compact accelerator.

Clearly then, the PBF system must be sufficiently portable to operate in the x-ray test room with automated operation from the control room. Its design should minimize the amount of metal in the x-ray path to the melt-pool. Experiments require a small number of fully fused layers to be deposited, over which a powder layer is spread in readiness for the x-ray pulse. The x-ray pulse is requested from the Vulcan control room, and PBF system laser is synchronized to scan across the powder bed and to be at the centre of the imaging region when the x-ray pulse arrives. It must be possible to deposit multiple layers automatically and remotely in order to monitor the development of pores between successive layers.

3. PBF system design

The open-architecture PBF system is shown in Figs. 1 and 2. It comprises a powder reservoir and spreader block that are moved as a single unit by a stepper motor and lead screw. The powder is gravity-fed and deposited in the build area as the spreader block moves linearly in one direction; the excess powder is removed as the spreader block returns. The build plates are 80 × 40 mm^2 coupons that are bolted to a rectangular support assembly that is rigidly connected to the vertical stage (z-axis). A circular hole in the support assembly leaves clear passage for the x-rays to pass from below the powder bed and will be discussed in more detail in the next paragraph. Powder layers of the desired thickness are produced by lowering the support assembly with the vertical stage (Standa 8MVT40-13-1, ~10 nm resolution). The rectangular support assembly moves as a 'piston' within the surface plate: a Teflon O-ring around the edge of the rectangular support prevents powder falling through the gap with the surface plate.

As noted above, the STFC Vulcan x-ray beam emerges horizontally into the test room with a total included angle of 40°: the desired x-ray beam diameter and direction are selected from within that cone with lead bricks. Two x-ray imaging directions are accommodated in the current design. The length of the slot in the spreader block can be set to <1 mm in the y-direction so that a thin line of powder is deposited in the x-direction. In this case, the PBF system is positioned so that the central region of the x-ray cone passes horizontally through the test region, as shown in Fig. 1(b). However, a

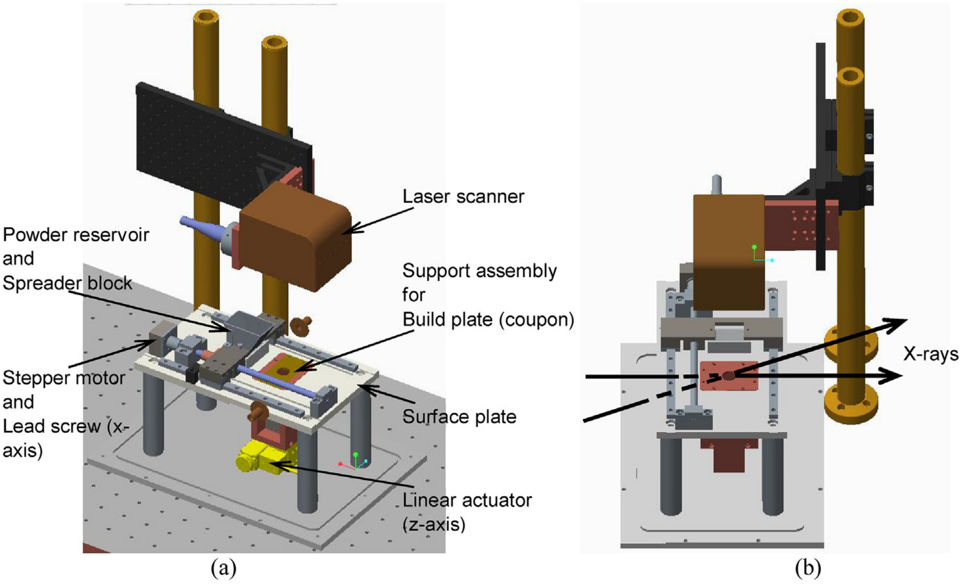

Fig. 1. (a) Schematic of the open-architecture powder bed fusion system. (b) Passage of x-rays, either at 12° to 57° to the horizontal, or horizontally, through the powder-bed.

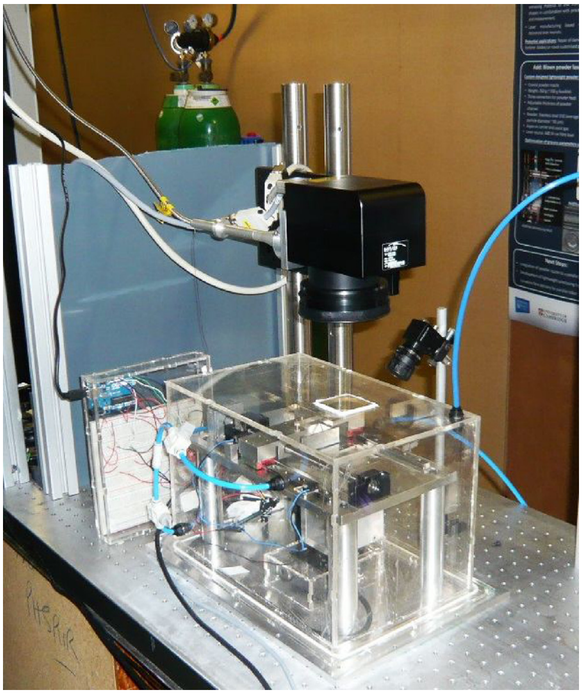

Fig. 2. Photograph of the open-architecture PBF system with the shielding gas chamber in position.

thin powder stripe is not representative of the heat flow away from the melt pool in the standard process, especially for multiple layer depositions. Hence a second mode of operation is enabled by the circular hole in the support assembly. In this case, the PBF system is raised so that the upper portion of the diverging cone of x-rays passes through the hole in the support assembly. X-rays making an angle of between 12 and 57° to the powder bed pass directly through the build coupon and powder layer, as shown in Fig. 1(b). X-rays outwith this range of angles are absorbed by the support assembly. This observation direction enables a powder layer of full width to be spread and the vertical 'edges' of the powder at the front and one side of the melt-pool to be imaged. For both imaging directions, the detector is placed ∼1.5 m behind the PBF system to yield a spatial resolution in the image of approximately 1 μm.

The powder in each layer is melted with light from a single mode fibre laser (SPI 400 W continuous wave, 1070 nm) which is scanned over the powder surface (Raylase MS-II-14 scanner with 163 mm focal length f-theta lens). A PC remotely controls the vertical movement of the support assembly, the movement of the powder spreader and the laser illumination and scanning. The build area on the coupon is approximately $30 \times 30\,\mathrm{mm}^2$. The maximum build depth is approximately 10 mm for the motion limit of the vertical stage. After processing, the metal coupons are removed for analysis.

The PBF system is enclosed in a detachable shielding gas chamber made of clear 5 mm thick Perspex sheet, of size $350 \times 230 \times 220\,\mathrm{mm}^3$ (Fig. 2). The shielding gas chamber is sealed to a baseplate using a Perspex flange and a silicon gasket (diameter 4 mm) that fits into a groove that runs completely around the baseplate. The chamber has inlet and exhaust ports for filling the shielding gas and providing a gas flow across the powder bed during builds. For a shielding gas that is heavier than air, the chamber is filled from a port close to the baseplate and the lighter air is exhausted from the port in the top surface of the chamber. When using a shielding gas that is lighter than air, the ports are reversed so that the lighter shielding gas enters at the top and expels the denser air from the bottom port. Once the oxygen concentration is reduced to <0.5% (measured using a Grove O_2 gas sensor) the shielding gas inlet is switched by an external valve to a second inlet port that is midway up the side of the shielding gas chamber to provide a constant flow across the powder bed during the build. A removable flow straightener (not shown) can be connected to the inlet port and mounted adjacent to the powder bed if required. The exhaust gas runs through a water bath to remove potentially harmful nanoparticles produced by the process. The laser beam passes through an anti-reflection coated UV-grade fused silica window in the top surface of the shielding gas chamber.

The key requirement of the spreading system is that it produces an accurate and repeatable powder layer thickness, and does not create excessive shear forces on previously deposited layers. Fig. 3 shows a cross-section of the spreading system at its midpoint. It comprises two main components: the carriage is supported on the rails and is driven backwards and forwards across the build coupon by the stepper motor and lead screw; and the spreader block that is connected to the carriage by fine pitch screws. The spreader block contains a V-shaped reservoir from which the powder is fed by gravity to sit between the two cylindrical spreaders. Clearly moving the whole reservoir is slower than spreading the powder with a separate wiper arm but an additional mechanism to deliver a metered dose of powder is avoided. Hence, gravity feed was chosen for simplicity and because build speed is not the primary concern for investigations into the process that involve single tracks and small build volumes. The design incorporates a piezoelectric shaker attached to the spreader block that can agitate the powder during spreading, but it has not been used in practice to date.

To deposit a layer, the carriage and spreader block move across the build plate in the forward spreading direction from the start position indicated in Fig. 3(b), and then return to the start position. The 'rear' spreader with respect to the forward spreading direction, on the left in Fig. 3(b), is 100 μm higher than the 'front' spreader. Hence the forward pass of the spreader block leaves an excess depth of 100 μm of powder that is scraped off by the front spreader as it returns to the start position. The depth of each powder layer is determined by the height of the front spreader above the surface plate, the amount the z stage moves down between layers plus the consolidation of the powder from the previous layer. The height of the front spreader is set by adjusting the height of the spreader block below the carriage with the fine pitch screws (0.5 μm per degree rotation): feeler gauges are inserted between the front spreader and the build plate to determine the height. We have tested tungsten carbide spreaders in the form of knife edges and cylinders. In both cases the spreader motion was jammed by the build-up of particles between the rigid spreader and the build plate. Therefore, we currently use silicon cord of diameter 3 mm.

The vertical movement of the platform, the movement of the powder spreader and the laser illumination and scanning are controlled remotely by PC. LabVIEW code takes as input the PBF process requirements such as number of layers and layer thickness and controls all aspects of depositing each powder layer. To start a build, the shield gas valves are activated remotely to fill the shielding chamber: when the O_2 sensor reports the desired concentration the shield gas is switched to flow across the build area. The code then drives the z-stage controller to lower by the amount required for a given powder layer depth. The motion of the powder spreader system is initiated: an Arduino Uno drives the lead screw forwards and then backwards until micro-switches attached to the extreme positions on the guide rail are activated. With a powder layer deposited, LabVIEW passes control to a SCAPS USC-2 card and SAMlight laser marking software which control the laser power and scanning unit. Hence the system has complete flexibility for laser power and speed, and scan geometry including hatching.

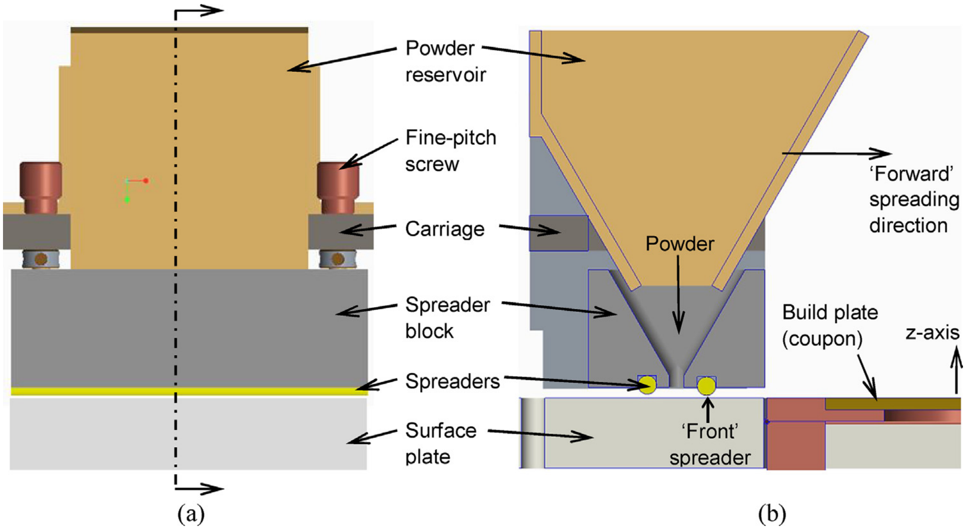

Fig. 3. Detail of powder spreading system. (a) Front view showing the powder spreader block mounted on its carriage with the fine pitch screws to adjust the height of the spreaders above the surface plate. (b) Side view (cross-section) showing the relative height of the spreaders above the surface plate.

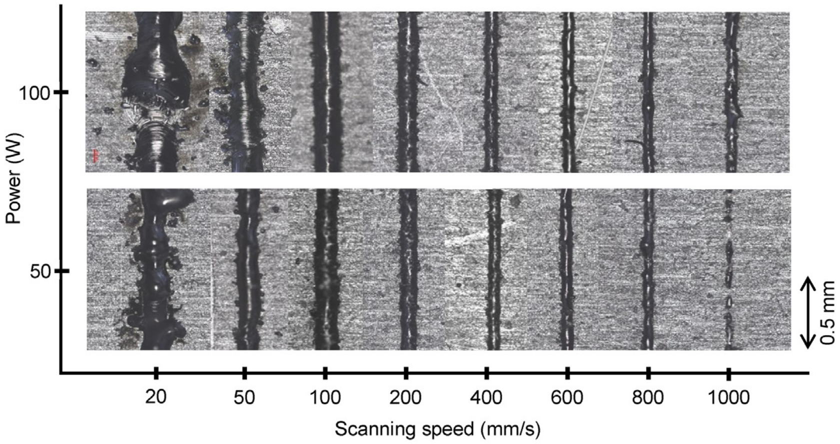

Fig. 4. Typical tracks at different laser scan speeds for laser powers of 50 and 100 W. Laser beam diameter 50 μm and powder layer thickness 50 μm.

4. Results

Whilst the design of the PBF system was originally determined by the requirements for x-ray access, portability and remote operation, the resulting open architecture design enables access for other in-situ measurements for fundamental process studies and for the development of process control. In this section, we validate that the PBF system produces single tracks and volume builds of acceptable quality to demonstrate that the process is representative for such measurements. For these experiments, we used gas-atomized stainless steel 316L powder (Renishaw PLC) with particle diameters in the range 15–45 μm and a mean diameter of 30 μm [18]. SS316L was chosen to validate the performance of the system because it has comparable properties to titanium but is significantly easier to handle. The $80 \times 40\,\text{mm}^2$ build plates (coupons) were made from 2 mm stainless steel (304L). For all the experiments reported, light from the laser was focussed to a spot with a Gaussian beam profile and 4Dσ diameter of 50 μm in both the x- and y-directions, measured with an Ophir Spiricon SP928 beam profiling camera.

Fig. 4 shows single tracks produced at different laser scanning speeds and two laser powers. A single powder layer of thickness 50 μm was spread directly on to the build coupon surface, where the thickness was set with the feeler gauge between the 'front' spreader and the build plate. Thinner tracks are produced as the laser power is decreased or the laser scan speed is increased. The thin tracks at the highest scan speeds demonstrate balling due to Plateau-Rayleigh instabilities in the molten metal and reduced penetration into the substrate. Conversely, the wider tracks at the lowest scan speeds are irregular and broken, with obvious spatter, due to the decreased viscosity at higher temperatures and instabilities in the melt-pool produced by the Marangoni flow. The tracks are continuous and straight for scan speeds from 100 to 400 mm/s at 50 W and 200 to 600 mm/s at 100 W.

For volume builds, the spreader height above the build plate was again set to 50 μm and the downwards motion of the z-stage between successive layers was set to 40 μm. For a laser power and scan speed of 50 W and 120 mm/s respectively, layers were built by scanning adjacent parallel tracks. The adjacent tracks in each layer were scanned in alternating directions. Between layers, the scan direction was rotated by 90°, i.e. parallel to the x-axis for odd layers and parallel to the y axis for even layers. Fig. 5(a) shows a staircase object built in this way. Fig. 5(b) shows a profile measurement for the staircase of the mean height across the step in the x-direction that was measured at each y-value when the staircase had been removed from the powder bed. The well-known edge effect [19], in which the first scanned line in a layer has a larger height than adjacent scans, is clearly seen in the odd-numbered layers where the scan in the x-direction is parallel to the edge of the step. The mean

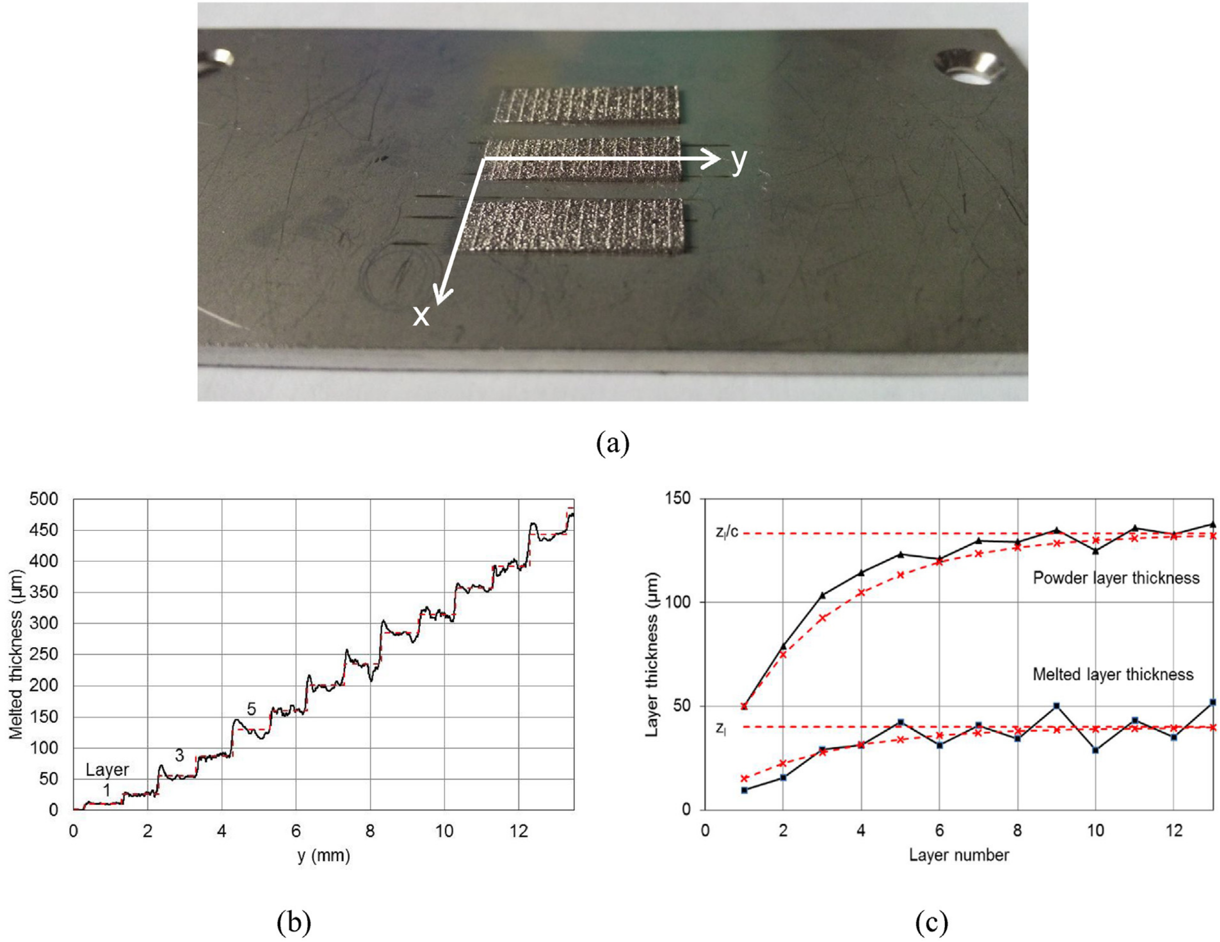

Fig. 5. (a) Staircase objects built to investigate powder layer shrinkage. (b) Mean height across the step in the x-direction (solid line) and mean height over each step (dashed line). (c) The measured thickness of each melted layer. Also shown is the powder layer thickness that produced each layer, calculated from the measured thickness of the preceding melted layer, the known downwards motion of the z-stage between layers (40 µm) and the height of the 'front' spreader above the build plate (50 µm). The dashed lines show the melted layer and powder layer thicknesses calculated using the powder consolidation of 0.3 calculated from Fig. 5(b).

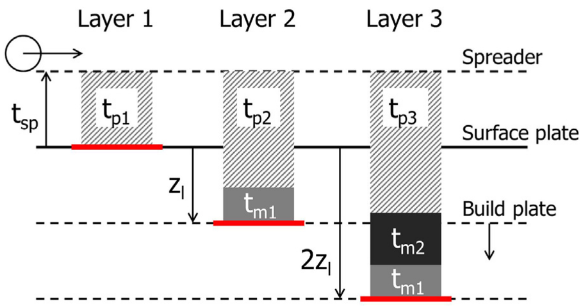

Fig. 6. Schematic of the powder layer thickness evolution for the first three layers. t_{sp} is the distance between the spreader and the surface plate and z_l is the z motion of the build plate for each layer. t_{pn} and t_{mn} are the powder and melted layer thicknesses, respectively, for layer n.

height of each step was calculated from the profile in Fig. 5(b) and is plotted in the figure as a dotted line. The powder layer thickness, and consequently the melted layer thickness, develop during the first few layers of a build until the steady state for the process is achieved. Fig. 5(c) shows the evolution of the melted layer thickness that was calculated as the difference between the mean height of consecutive layers from the measurements in Fig. 5(b).

The evolution of the powder layer and melted layer thicknesses for the first three layers is shown schematically in Fig. 6. Each layer in the figure shows the spread powder thickness prior to melting it. For layer 1, the powder layer thickness, t_{p1}, corresponds to the height of the spreader above the build plate, t_{sp}. In our system, the spreader was adjusted to be 50 µm above the surface plate with a feeler gauge, and the surface plate and built plate (coupon) surfaces were adjusted to the same height, giving $t_{p1} = t_{sp} = 50$ µm. For layer 2, the build plate surface moves down by z_l and the powder layer thickness now corresponds to the height of the spreader above the build plate, t_{sp}, plus the difference between the z_l and the thickness of the first melted (consolidated) layer, t_{m1}. Similarly for layer 3, the build plate surface has moved down an additional step of z_l and the powder layer thickness changes by z_l-t_{m2}, where t_{m2} is the thickness of the second melted layer. In this way, it is straightforward to show that the powder layer thickness for layer n for $n \geq 2$ is given by the geometric series:

$$t_{pn} = t_{sp} + \left(z_l - ct_{sp}\right) \sum_{i=0}^{n-2} (1-c)^{\,i} \qquad (1)$$

where $c = t_{mn}/t_{pn}$ is the consolidation ratio that relates the thickness of a melted layer produced by shrinkage of the powder layer. The change in powder layer thickness between consecutive layers, $\left(z_l - ct_{sp}\right) \ (1-c)^{\,n-2}$ tends to zero. Therefore the powder layer thickness in the steady state can be determined by summing the geometric series in Eq. (1) to infinity:

$$t_p = t_{sp} + \left(z_l - ct_{sp}\right) \frac{1}{1-(1-c)} = \frac{z_l}{c} \qquad (2)$$

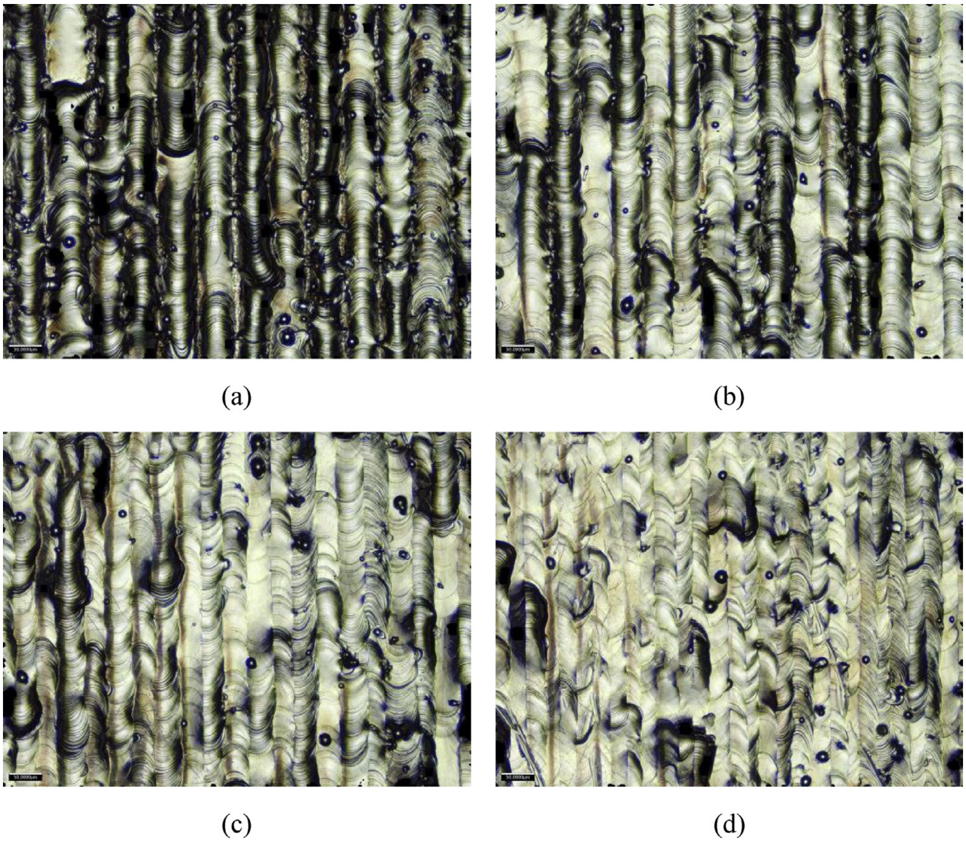
(a) (b) (c) (d)

Fig. 7. Optical microscope images of melted areas with scan spacing factors of a) 1.1 (110 μm), b) 0.9 (90 μm), c) 0.7 (70 μm) and d) 0.5 (50 μm) for laser power 50 W, scan speed 120 mm/s, laser spot diameter 50 μm and powder layer thickness 50 μm.

The melted powder thickness is obtained by multiplying Eq. (1) by c, so that the melted layer thickness is

$$t_{mn} = ct_{sp} + c\left(z_l - ct_{sp}\right)\sum_{i=0}^{n-2}(1-c)^{i} \qquad (3)$$

and the melted layer thickness is in the steady state is $t_m = z_l$.

The measured melted thickness for each layer in the staircase object in Fig. 5(b) enables the thickness of the subsequent powder layer spread over it to be calculated from the known spreader height above the build plate $t_{sp} = 50\ \mu m$ and the build step increment of $z_l = 40\ \mu m$. The powder layer thickness calculated for each layer is shown in Fig. 5(c). The consolidation ratio for each layer can then be calculated, and its mean value was approximately 0.3. Fig. 5(c) includes the melted layer thickness and powder layer thickness, calculated from Eqs. (3) and (1) respectively, for these experimental values of t_{sp}, z_l and c. Steady state melted layer thickness of $t_m = z_l = 40\ \mu m$, and powder layer thickness of $t_p = z_l/c = 133\ \mu m$ are established after approximately 10 layers.

For volume builds, an acceptable distance between parallel adjacent tracks in each layer, the scan spacing *s*, was determined by experiment. For laser power and scan speed of 50 W and 120 mm/s, specimens were produced with scan spacing reduced from 110 μm to 50 μm in steps of 20 μm. These scan spacing values corresponded to scan spacing factors *s/2d* of between 1.1 at 110 μm and 0.5 at 50 μm, where *d* is the laser spot diameter. The surface quality of each specimen was inspected under an optical microscope, Fig. 7, and the surface profile was measured orthogonal to the adjacent tracks, Fig. 8. For a scan spacing factor of 1.1 the tracks are clearly separated and no overlapping is observed. The surface flatness only increases marginally in passing from a scan spacing factor of 0.7–0.5 with an approximate 20% increase in processing time.

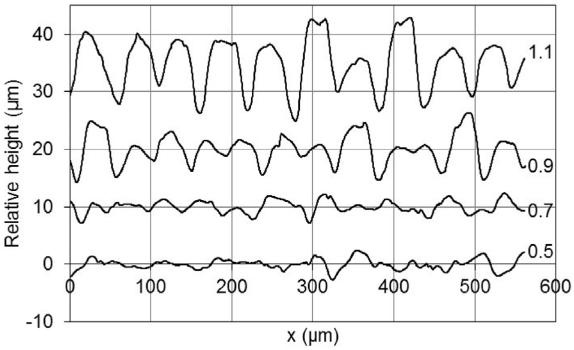

Fig. 8. Surface profile measured along a line at the centre of the microscope images shown in Fig. 7. An offset of 10 μm, 20 μm and 30 μm has been added to the lines for scan spacing factor 0.7, 0.9 and 1.1 respectively, in order to separate the lines on the graph.

Three cubes of size 5 × 5 × 5 mm^3 were manufactured on a single coupon with scan spacing factors of 1.1, 0.9 and 0.7 and with the same laser parameters, Fig. 9a. The build time of the components was around 1.5 h, which is dominated by the scan speed of the powder spreader which was ~10 mm/s. Three such coupons were produced, making a total of 9 cubes, i.e. three cubes at each scan spacing factor. The cubes were separated from the build coupon using a low speed diamond cutter. The density of each of the nine cubes was measured by applying Archimedes' immersion method following the procedure described in Ref. [20]. We used a KERN analytical balance (AJS/ACS, resolution ±0.1 mg) with a den-

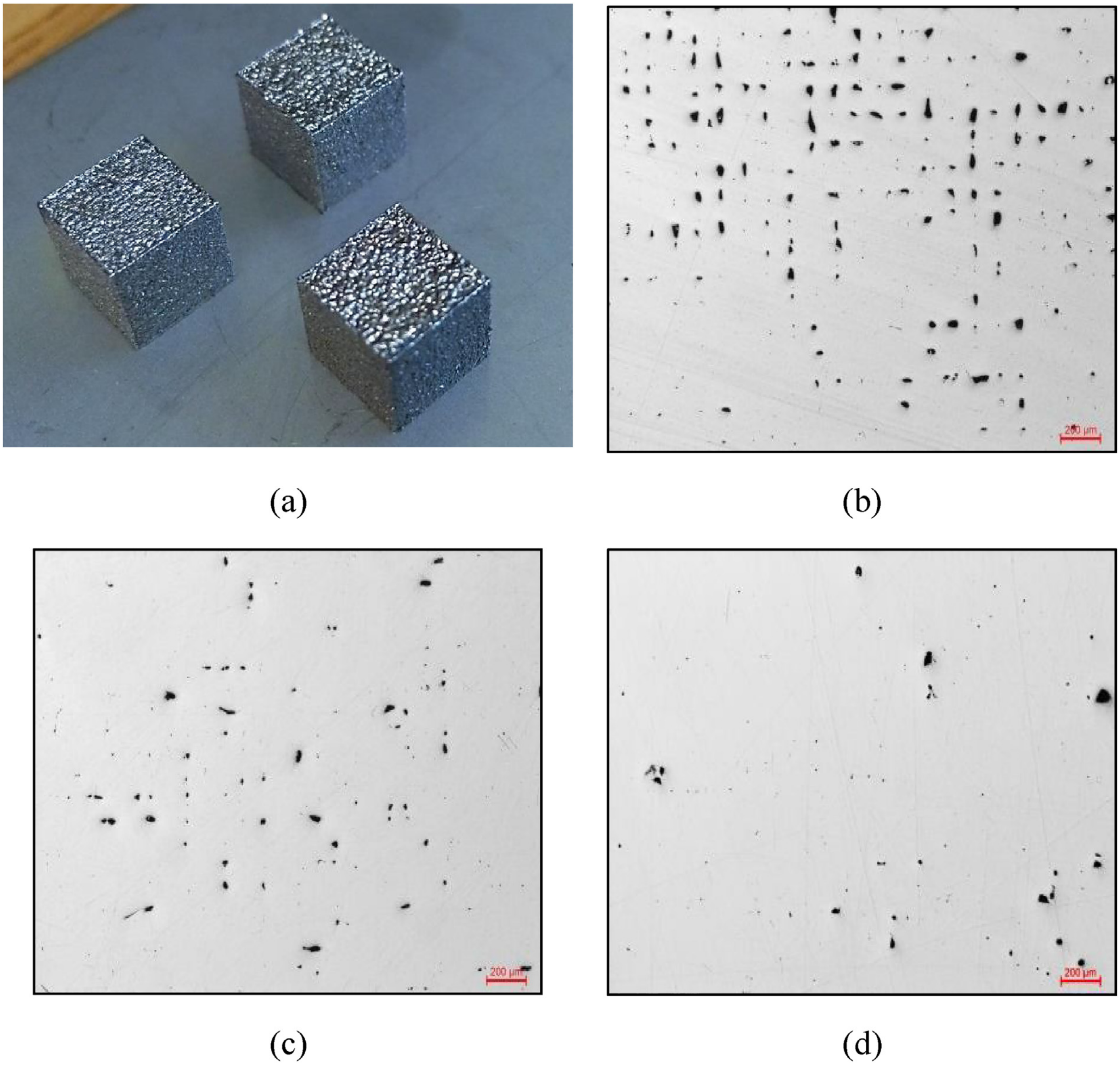

Fig. 9. Effect of scan spacing factor on component density. (a) Cube samples for density measurements. (b) Microscope images of sectioned cubes at ×5 magnification for scan spacing factors of (b) 1.1, (c) 0.9 and (d) 0.7.

sity measurement attachment for solid materials (ABT-A01) and deionised water as the immersion fluid. The density is expressed as a percentage of the density of bulk stainless steel 316L (7.9 g/cm^3). Air buoyancy was included in the calculation [21] which typically reduces the density by approximately 0.1% compared to the non-corrected value. A density exceeding 99% was achieved for a scan spacing ratio of 0.7, Fig. 10(a).

One cube for each scan spacing ratio was sectioned, embedded in epoxy resin and polished using diamond suspension paste. Optical micrographs at ×5 magnification were recorded from the centre of the cubes, Fig. 9(b)–(d). At the largest scan spacing factor of 1.1, the pores are uniformly distributed in a regular pattern due to insufficient overlapping of the individual single tracks resulting in a low density. The micrographs show the increase in density with decreasing scan spacing factor. At 0.9 scan spacing factor the overlap of adjacent tracks is close to a threshold where any necking (thinning) of a track results in porosity. At 0.7 scan spacing factor, the track overlap was sufficient to accommodate any track necking without loss of track overlap. These images were analysed in ImageJ to measure the area of pores, and the values expressed as a percentage are plotted in Fig. 10(b). Again, a density >99% was measured for a scan spacing factor of 0.7. Both Fig. 10(a) and (b) indicate that a further increasing in the scan spacing factor might improve the density still further if required, but obviously at the expense of an increased processing time and residual stresses (due to increased heat input per unit volume of powder). We have found that the density measured by immersion produces a systematically lower result than by imaging and that this is consistent with other studies using optical and SEM imaging, Fig. 10(c). In general, the Archimedes method gives the fastest measurement although obviously no information is obtained regarding the distribution of defects.

Fig. 11 shows four complex shapes built with the system. The CAD model was prepared using Creo 2.0, sliced using the open source software Slice3r and each sliced geometry processed on the PBF system using the SCAPS scan software. Processing parameters were chosen based on the previous experiments: power 50 W, scanning speed 120 mm/s, scan spacing factor 0.7 and a stable powder layer thickness of 130 μm. The built components were inspected

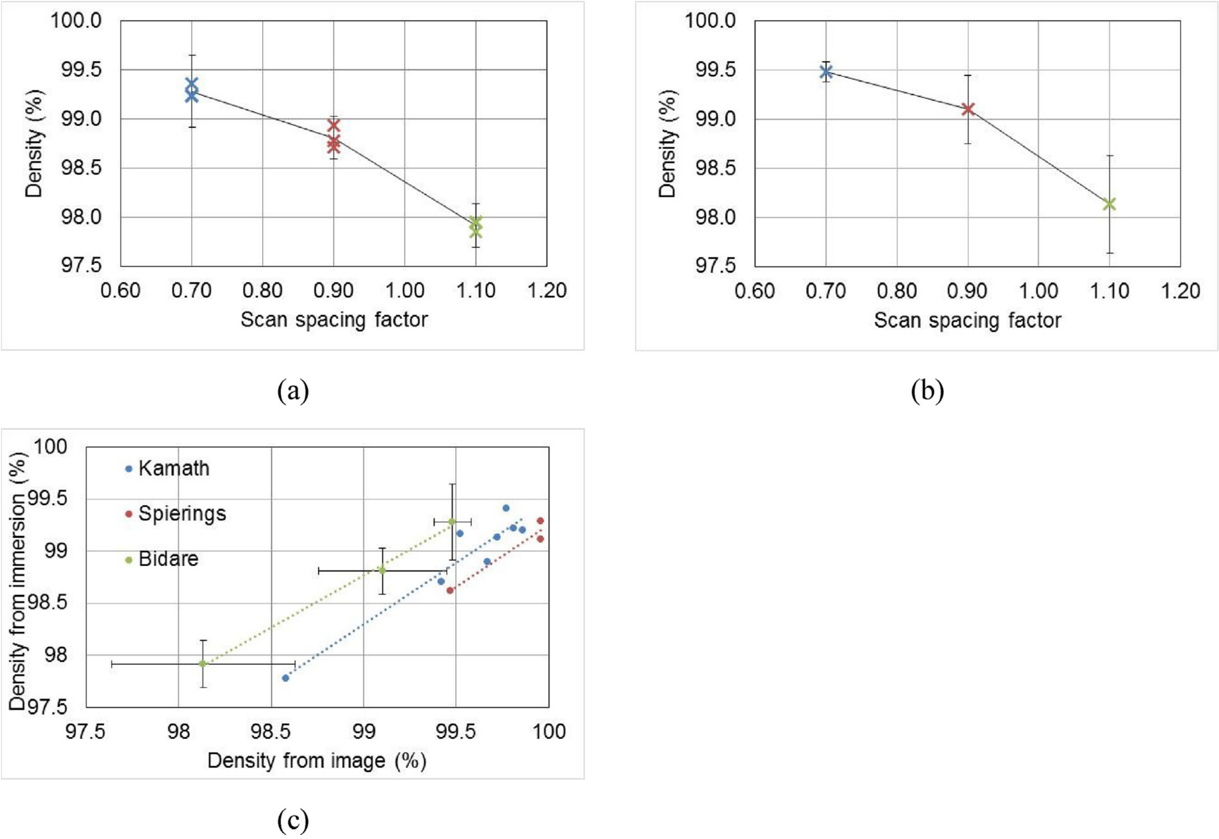

Fig. 10. Effect of scan spacing factor on component density. Density measurements using (a) Archimedes immersion method (3 cubes at each scan spacing factor) and (b) analysis of optical microscope images (one cube at each scan spacing factor). (c) Relationship between density measurement methods including a comparison with results reported by Kamath [21] and Spierings [20].

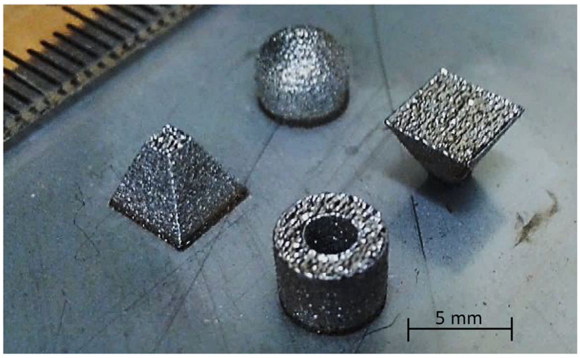

Fig. 11. Cylinder, dome, pyramid and inverted pyramid produced by the open architecture PBF system. Each component is contained in a cube of 5 × 5 × 5 mm^3.

visually and found to be of good quality with almost no outside defects. The depth of the components was 5 mm or approximately 125 layers. The dimensional accuracy, in particular heights, widths and diameters, were checked with a CMM and were accurate to within ±0.1 mm. The surface finish was measured with the Alicona profilometer: the top surface finish <20 μm Rz and side surface finish <25 μm Rz.

The open architecture of the system has enabled high-speed image sequences of the PBF process to be recorded with possibly the highest quality to date, for single track, area and multilayer builds. Schlieren imaging of the laser plume and inert atmosphere above the powder bed has also been undertaken, we believe for the first time. Still images from the video sequences are shown in Fig. 12. The results from these experiments, and the understanding of process fundamentals provided by them, are being prepared for publication. The x-ray source at STFC is set up for approximately two weeks each summer for imaging applications. Experiments were scheduled in the summers of 2015 and 2016 but unfortunately issues with the x-ray source meant that on both occasions no imaging with the PBF system could be attempted. We plan experiments at STFC in the future, but the limited availability of the x-ray source during the year makes obtaining results somewhat difficult. We are currently investigating access to x-ray and synchrotron sources at other facilities where the flexible design of the PBF system should enable it to be used with minimum modifications.

5. Conclusion

A compact and automated system for powder bed fusion additive manufacture has been reported. Its design was determined by the requirements for x-ray access, portability and remote operation. In particular, the system can accommodate both horizontal viewing through a very thin powder bed, and oblique imaging at 12–57° from the horizontal from below the powder bed through a full-width powder bed for more representative heat conduction. In both cases, single track, area and multiple layer builds can be implemented automatically. The system was characterized and it was demonstrated that parts with >99% density are produced by the system. The design is simple and very few components require precision machining, making it an approach that is accessible to most research groups. Furthermore, its open-architecture design enables access to the build area for a range of other in-situ measurement techniques: we are currently using the system for high-speed imaging, shield gas flow and temperature measurements. It is also being used to test new laser sources and for testing new materials because only small volumes of powder are required.

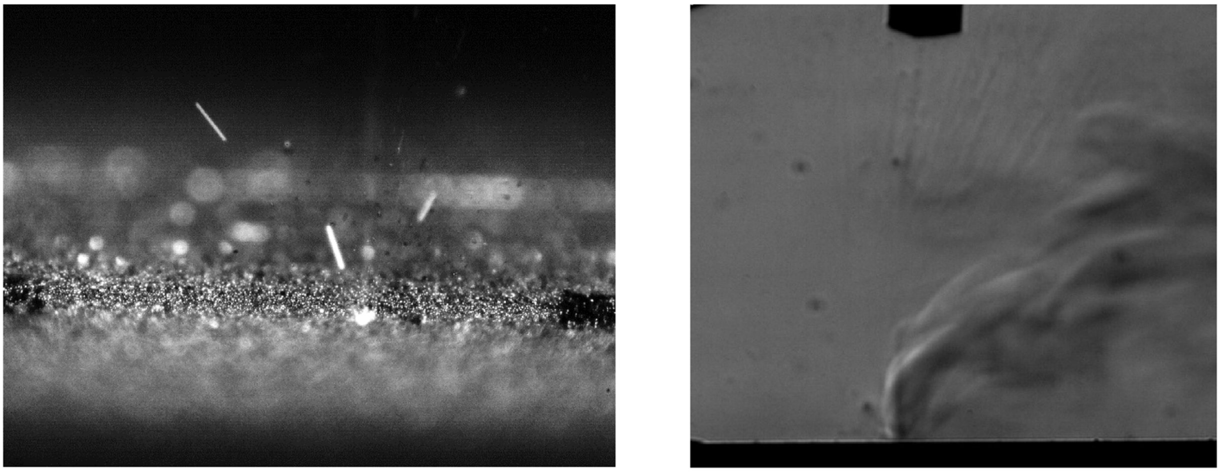

(a)

(b)

Fig. 12. Examples of in-situ process measurements enabled by the PBF system. (a) Still image from high-speed image sequence of laser spot traversing the powder bed. (b) Schlieren image from video sequence showing the interaction of the laser plume with the shielding gas flow across the powder bed. In both cases the laser is scanning across the powder bed towards the camera.

Acknowledgements

This work was supported by the Engineering and Physical Sciences Research Council (Grant numbers EP/I033335/2 and EP/K030884/1). The authors acknowledge useful discussions with Joe Kelleher (STFC), Andrew Bayly (Leeds University), Phil Prangnell (Manchester University) and Nick Jones (Renishaw PLC) during this work. Access to the Vulcan laser x-ray source was arranged by Joe Kelleher, Ceri Brenner and Ric Allott through the STFC Harwell Imaging Partnership, which aims to identify potential applications in advanced imaging and non-destructive testing of x-ray sources at the Central Laser Facility. Relevant research data presented in this publication can be accessed at http://dx.doi.org/10.17861/ab961f91-d27f-471e-a0eb-6f9ab0571f64.

References

[1] I. Gibson, D.W. Rosen, B. Stucker, Additive Manufacturing Technologies, 2010.

[2] I. Yadroitsev, P. Bertrand, I. Smurov, Parametric analysis of the selective laser melting process, Appl. Surf. Sci. 253 (2007) 8064–8069.

[3] P. Edwards, A. O'Conner, M. Ramulu, Electron beam additive manufacturing of titanium components: properties and performance, J. Manuf. Sci. Eng. 135 (2013) 061016-1–061016-7.

[4] K.A. Mumtaz, N. Hopkinson, P. Erasenthiran, High density selective laser melting of Waspaloy, Solid Free. Fabr. Symp. (2006) 220–232.

[5] W.E. King, H.D. Barth, V.M. Castillo, G.F. Gallegos, J.W. Gibbs, D.E. Hahn, C. Kamath, A.M. Rubenchik, Observation of keyhole-mode laser melting in laser powder-bed fusion additive manufacturing, J. Mater. Process. Technol. 214 (2014) 2915–2925.

[6] A.B. Spierings, N. Herres, G. Levy, C. Buchs, Influence of the particle size distribution on surface quality and mechanical properties in additive manufactured stainless steel parts, Rapid Prototyp. J. 17 (2011) 195–202, Spec. Issue SFF 2010.

[7] B. Liu, R. Wildman, C. Tuck, I. Ashcroft, R. Hague, Investigation the effect of particle size distribution on processing parameters optimisation in selective laser melting process, Solid Free. Fabr. Proc. (2011) 227–238.

[8] J.P. Kruth, L. Froyen, J. Van Vaerenbergh, P. Mercelis, M. Rombouts, B. Lauwers, Selective laser melting of iron-based powder, J. Mater. Process. Technol. 149 (2004) 616–622.

[9] I. Yadroitsev, L. Thivillon, P. Bertrand, I. Smurov, Strategy of manufacturing components with designed internal structure by selective laser melting of metallic powder, Appl. Surf. Sci. 254 (2007) 980–983.

[10] C. Simonelli, I. Aboulkhair, I. Maskery, R.D. Wildman, R. Hague, A study on the laser spatter and the oxidation reactions during selective laser melting of 316L stainless steel, Al-Si10-Mg, and Ti-6Al -4V, Metall. Mater. Trans. A 46 (September (9)) (2015) 3842–3851.

[11] T. Craeghs, S. Clijsters, E. Yasa, J.-P. Kruth, Online quality control of selective laser melting, Solid Free. Fabr. Proc. (2011) 212–226.

[12] T.B. Sercombe, X. Xu, V.J. Challis, R. Green, S. Yue, Z. Zhang, P.D. Lee, Failure modes in high strength and stiffness to weight scaffolds produced by Selective Laser Melting, Mater. Des. 67 (2015) 501–508.

[13] M.L. Vlasea, B. Lane, F. Lopez, S. Mekhontsev, A. Donmez, Development of powder bed fusion additive manufacturing test bed for enhanced real-time process control, Solid Free. Fabr. Proc. (2015) 527–539.

[14] W.S. Land, B. Zhang, J. Ziegert, A. Davies, In-situ metrology system for laser powder bed fusion additive process principle of operation, Procedia Manuf. 1 (2015) 393–403.

[15] R.D. Edwards, M.A. Sinclair, T.J. Goldsack, K. Krushelnick, F.N. Beg, E.L. Clark, A.E. Dangor, Z. Najmudin, M. Tatarakis, B. Walton, M. Zepf, K.W.D. Ledingham, I. Spencer, P.A. Norreys, R.J. Clarke, R. Kodama, Y. Toyama, M. Tampo, Characterization of a gamma-ray source based on a laser-plasma accelerator with applications to radiography, Appl. Phys. Lett. 80 (2002) 2129–2130.

[16] A.M. Shaikh, C. Romesh, T.S. Kolage, A. Sharma, Flash x-ray radiography with phosphor imaging plate, E-J. Nondestruct. Test. 20 (2015) 2–9.

[17] C.M. Brenner, S.R. Mirfayzi, D.R. Rusby, C. Armstrong, A. Alejo, L.A. Wilson, R. Clarke, H. Ahmed, N.M.H. Butler, D. Haddock, A. Higginson, A. McClymont, C. Murphy, M. Notley, P. Oliver, R. Allott, C. Hernandez-Gomez, S. Kar, P. McKenna, D. Neely, Laser-driven x-ray and neutron source development for industrial applications of plasma accelerators, Plasma Phys. Control. Fusion 58 (2016) 014039.

[18] P.L.C. Renishaw, Data Sheet SS 316L-0410 Powder for Additive Manufacturing, 2016, www.renishaw.com/en/data-sheets-additive-manufacturing–17862. (Accessed 15 December 2016).

[19] I. Yadroitsev, I. Smurov, Surface morphology in selective laser melting of metal powders, Phys. Procedia 12 (2011) 264–270.

[20] A.B. Spierings, M. Schneider, R. Eggenberger, Comparison of density measurement techniques for additive manufactured metallic parts, Rapid Prototyp. J. 17 (2011) 380–386.

[21] C. Kamath, B. El-dasher, G.F. Gallegos, W.E. King, A. Sisto, Density of additively-manufactured, 316L SS parts using laser powder-bed fusion at powers up to 400 W, Int. J. Adv. Manuf. Technol. 74 (2014) 65–78.